# First accuracy evaluation of the NRC-FCs2 primary frequency standard

**Scott Beattie**[1] , **Bin Jian**[1] , **John Alcock**[1], **Marina Gertsvolf**[1] , **Rich Hendricks**[2] , **Krzysztof Szymaniec**[2] **and Kurt Gibble**[3]

[1] National Research Council Canada, Ottawa, ON, K1A 0R6, Canada
[2] National Physical Laboratory, Hampton Road, Teddington, TW11 0LW, United Kingdom
[3] Department of Physics, The Pennsylvania State University, University Park, PA 16802, United States of America

E-mail: Scott.Beattie@nrc-cnrc.gc.ca

CrossMark

## Abstract

We report the first accuracy evaluation of NRC-FCs2, an atomic fountain clock developed at the National Research Council Canada. The short term stability at high atomic density is $1.1 \times 10^{-13}$ at 1 second of averaging time. The typical overall fractional type B uncertainty is $2.3 \times 10^{-16}$. GNSS-based frequency comparisons of NRC-FCs2 with the SI second, as reported by the BIPM over fourteen months, give a fractional frequency difference of $-2.4(3.7) \times 10^{-16}$.

Keywords: primary frequency standard, atomic clock, GNSS frequency comparison, cold atoms

(Some figures may appear in colour only in the online journal)

## 1. Introduction

Primary frequency standards (PFSs) hold particular importance in the world of metrology. In addition to serving as the reference for frequency and time, accurate measurement of the SI second is fundamental in the definitions and practical realizations of all other SI base units, with the exception of the mole. Since the first caesium fountain primary frequency standard was realized using laser-cooling and trapping techniques [1, 2], these devices have become fundamental to atomic timekeeping. Through continued advances, fountain clocks have now reached relative uncertainties at the level of $10^{-16}$ [3–10], exhibiting accuracy over an order of magnitude higher than thermal beam clocks.

International Atomic Time (TAI) is currently steered by primary and secondary frequency standards operated in several national laboratories around the world. As caesium fountain clocks provide the most accurate realization of the SI second, their contribution dominates the weighted steering of TAI. Many laboratories have evaluated, or are currently evaluating, caesium fountain PFSs, however, typically only a few report to the International Bureau of Weights and Measures (BIPM) at any given time. This demonstrates the need for more fully-evaluated caesium fountain clocks to report regularly to maintain a stable and robust international timescale.

At the National Research Council Canada (NRC), we have completed the first accuracy evaluation of the primary frequency standard, NRC-FCs2. This fountain clock incorporates refurbished optical, microwave, and electronics subsystems from NRC-FCs1 [11], as well as a new physics package. NRC-FCs2 will serve as a PFS to help provide an accurate local timescale in Canada, contribute to the steering of TAI, and will support the NRC's ongoing development of next-generation optical clocks [12, 13].

## 2. Description of NRC-FCs2

### 2.1. Physics package

The physics package of NRC-FCs2 was built at the National Physical Laboratory (NPL) in the UK and is based on the design of the NPL-CsF2 and NPL-CsF3 fountain clocks [4, 14]. It is described in detail in [15] and is shown in figure 1. The physics package consists of a lower region containing the chamber for the magneto-optical trap (MOT), optical pumping, and state detection; and a magnetically-shielded upper region that contains the microwave cavities and the flight chamber.

The MOT is vapour-loaded from a caesium reservoir that consists of two 1-gram caesium ampoules placed inside an
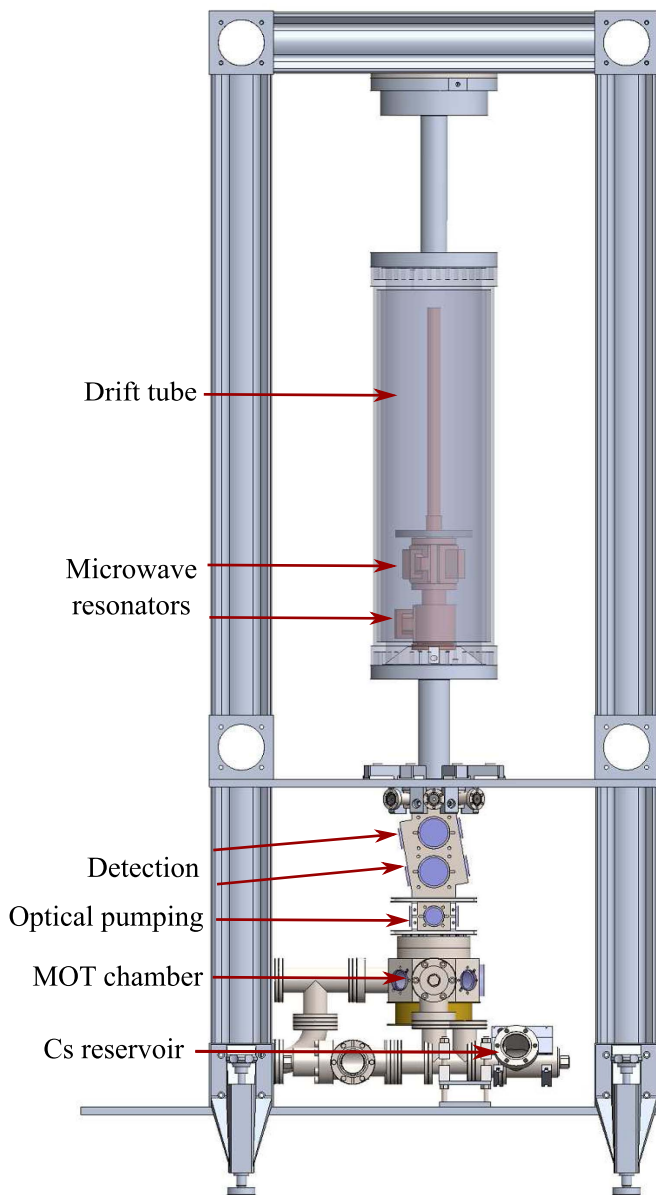
**Figure 1.** Diagram of the NRC-FCs2 physics package.

all-metal valve. After baking out the vacuum system, the larger-diameter ampoule was crushed by partially closing the valve, leaving the second ampoule in reserve. The temperature of the reservoir is controlled with a thermoelectric cooler (TEC) attached to the valve to maintain the Cs vapour pressure at the desired level. The reservoir is typically cooled to ∼4 °C and a recirculating water cooling unit is used to extract heat from the TEC.

The fountain uses a (0,0,1) cooling beam geometry with laser light delivered by optical fibers. The fibers are connected to the vacuum system via optomechanical cage systems to facilitate alignment. A pair of coils in anti-Helmholtz configuration provides the quadrupole magnetic field for the MOT stage. Two optical ports located 10 cm above the MOT chamber provide access for optical pumping light in the horizontal plane. A pair of coils in Helmholtz configuration produces a bias field to define the quantization axis during optical

pumping. The detection light is delivered by optical fiber to a cage system mounted directly to the vacuum chamber.

The state selection cavity is cylindrically symmetric with a single feed. The Ramsey cavity, however, has four feeds (separated by 90° azimuthally around the cavity midplane). This facilitates the evaluation of the distributed cavity phase (DCP) shift as it is enables feeding the microwaves in a fully symmetric/asymmetric manner along orthogonal transverse axes of the cavity. During normal operation, however, only two balanced and opposing feeds are used. The Ramsey cavity geometry minimizes the DCP shift, and has tapered endcaps with 14-mm-diameter apertures [16, 17]. The loaded quality factor of the Ramsey cavity is $Q_L = 15000$ and the resonance frequency is kept within 30 kHz of the caesium ground state hyperfine transition frequency via temperature control.

The double-walled aluminum flight chamber serves as a water jacket, used to stabilize the temperature within the chamber. The chamber contains the state selection and Ramsey cavities. Above the Ramsey cavity, there is a 40 cm-long copper below-cutoff waveguide to suppress perturbations from microwave leakage. Water from a temperature-controlled chiller is cycled through the water jacket to stabilize the temperature of the flight tube and microwave cavities. The vertical C-field is provided by a 72 cm long double-wound solenoid that extends 53 cm above the Ramsey cavity. The flight tube is contained within three layers of mu-metal shielding, which collectively provide a shielding factor of ∼200 000.

Ultra-high vacuum is maintained at the $10^{-10}$ mbar level by three ion pumps and two getter pumps; two 20 ls$^{-1}$ ion pumps and one getter pump are located below the MOT chamber and one 8 ls$^{-1}$ ion pump and one getter pump are at the top of the flight chamber. The getter pumps also helped to maintain low vacuum pressure while the physics package was transported from NPL to NRC without electrical power. Background caesium pressure is reduced by graphite installed at the aperture between the MOT region and the drift tube. Additional graphite tubes installed near the ion pump inlets help to extend the lifetime of the pumps.

## 2.2. Lasers and optical system

The optical layout is shown in figure 2. The light required for laser-cooling and trapping, optical pumping, and state detection is provided by a 12 mW external-cavity diode laser (ECDL) and two tapered amplifiers. The ECDL has a nominal linewidth of < 200 kHz and is amplified to 150 mW using the first tapered amplifier ($TA_1$). At the output of $TA_1$, a portion of the light is directed to a saturated-absorption spectroscopy (SAS) setup which uses two balanced photodiodes to produce a Doppler-free SAS signal. The pump beam is frequency-shifted [18] by −125 MHz and modulated at 350 kHz using an acousto-optic modulator (AOM) in a double-pass configuration. The ECDL is locked to the $|F = 4\rangle \rightarrow |F' = 4, 5\rangle$ Cs $D_2$ crossover peak of the frequency-shifted SAS signal; an energy level diagram for $^{133}$Cs indicating the relevant transitions is shown in figure 3. This leaves the ECDL laser output unmodulated and detuned by −62.5 MHz with respect to the $|F = 4\rangle \rightarrow |F' = 5\rangle$ cycling transition, $f_{45}$. Another portion
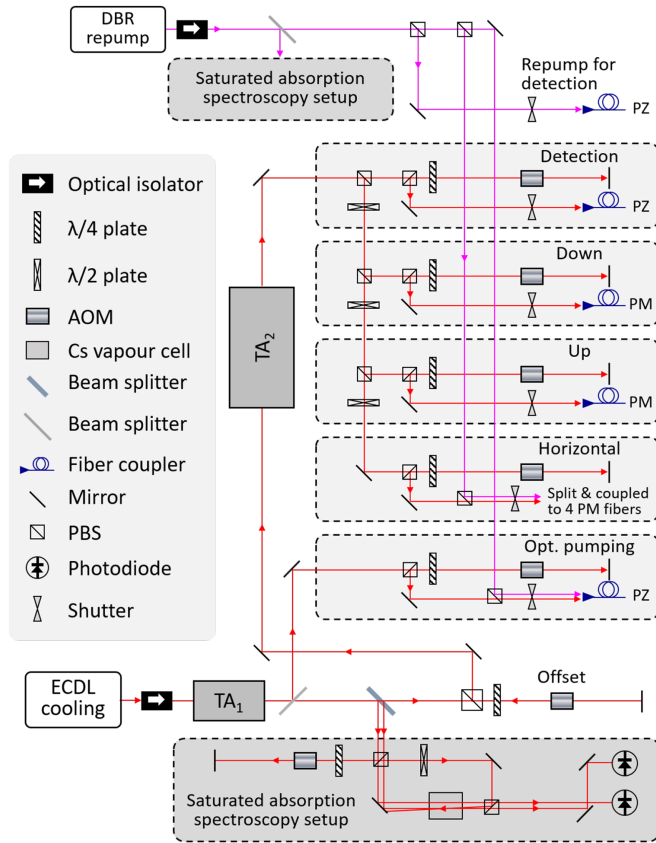
**Figure 2.** Diagram of the optical setup.



**Figure 3.** Energy levels of $^{133}$Cs.

of the light from $TA_1$ is sent to a second double-pass AOM to shift the light on resonance with the $f_{44}$ optical pumping transition. This light is then delivered to the physics package via polarizing (PZ) fibers after being combined with $\sim$100 µW of repump light, resonant with $f_{34}$. The remaining light from the $TA_1$ is frequency shifted by $\sim$ −140 MHz by a double-pass "Offset" AOM, further shifting the light to 202.5 MHz below $f_{45}$ before being used to seed a second tapered amplifier ($TA_2$), which outputs (600–1000) mW.

The output of $TA_2$ is split and sent to 4 double-pass AOMs to control the state detection light, as well as the "Up", "Down", and "Horizontal" cooling light. The double-pass AOM for the detection light shifts the laser frequency back to $f_{45}$ before the light is delivered to the physics package via PZ fiber. Light from the 3 double-pass AOMs used for laser-cooling is shifted up by 189 MHz, leaving the MOT light −13.5 MHz detuned with respect to $f_{45}$ to optimize Doppler cooling. The light is delivered to the physics package via polarization-maintaining (PM) fibers. During the molasses cooling stage, the frequencies of the "Offset", "Up", "Down", and "Horizontal" AOMs are all ramped to leave the cooling light detuned by −66.5 MHz with respect to $f_{45}$. At the MOT region, each cooling beam has (10–15) mW of power with a $\sim$2 cm beam diameter, with the exception of the "Down" cooling beam, which is limited by the 14 mm microwave cavity apertures. All fibers are connected to opto-mechanical cage systems mounted directly to the vacuum system, which simplifies initial alignment and provides robust pointing stability.
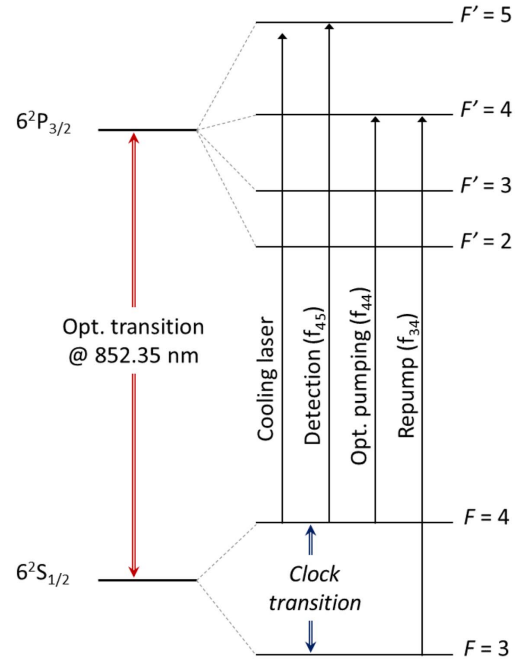
A distributed Bragg reflector (DBR) laser produces $\sim$35 mW of repump light for the MOT, optical pumping, and state detection. A small fraction of the light ($\sim$1 mW) is sent to a saturated-absorption spectroscopy setup where the pump beam is frequency-shifted by +201 MHz and modulated using an AOM in a double-pass configuration. The probe beam is locked to the $|F=3\rangle \rightarrow |F'=3,4\rangle$ saturated absorption crossover peak, leaving the unmodulated laser output on resonance with the $f_{34}$ repump transition. The compact and robust laser design leads to excellent frequency stability and both the cooling and repump lasers maintain their frequency locks for months without intervention.

The light used for fluorescence state detection is tuned to the $|F=4\rangle \rightarrow |F'=5\rangle$ cycling transition and is split and combined with repump light in the lower detection region using polarizing beam splitter (PBS) cubes. It is collimated using a system of spherical and cylindrical lenses and is delivered to the physics package at an angle of 10° with respect to the horizontal plane. This causes the detection light to be Doppler shifted off-resonance for thermal background atoms entering the detection region from the MOT chamber, thereby reducing the background fluorescence [15]. The wings of the detection beams are masked in the horizontal plane such that the detection light has a width of 16 mm and an intensity that is uniform within 5%. The detection light intensity is stabilized with a 100 kHz servo controlling the RF power driving an AOM. The light is retro-reflected to create a standing wave, however, the bottom $\sim$5 mm of the upper detection light is masked at the retro-reflecting mirror to create a traveling-wave "pusher" beam to remove the $F=4$ atoms after detection in the upper region. The fluorescence is focused onto two photodetectors (one for each detection region), which are mounted onto the detection chamber, orthogonal to the detection light. The collected fluorescence is effectively doubled by mounting

a collimating lens and a retro-reflecting mirror to the detection chamber, opposite to each photodetector. This results in fluorescence collection with an effective solid angle of 3.8 sr.

### 2.3. Microwave source

To produce the Ramsey microwaves used to probe the atoms, we use a CS-1 model synthesizer from SpectraDynamics Incorporated. This unit contains 5 MHz and 100 MHz voltage-controlled crystal oscillators (VCXO), a dielectric resonant oscillator (DRO) with 9.2 GHz output, and a 48 bit direct digital synthesizer (DDS) that produces a programmable RF frequency near 7.3 MHz. The output of the DRO is mixed with the output of the DDS to generate a variable frequency near the caesium $|F = 3\rangle \rightarrow |F = 4\rangle$ clock transition, at $f_0 \equiv 9\,192\,631\,770$ Hz.

The VCXOs in the synthesizer are weakly phase-locked to an active hydrogen maser, VM1, manufactured by Vremya-CH (VCH-1003M, option L). The DDS is computer-controlled through RS232 communication to adjust the microwave frequency and lock it to the central Ramsey fringe. Therefore, in normal clock operation, the frequency of VM1 is measured against NRC-FCs2.

### 2.4. Fountain operation

The experimental cycle of NRC-FCs2 consists of five steps: atomic sample preparation, launch, state preparation, microwave interactions and free evolution (Ramsey time), and atomic state detection. The MOT is formed at the intersection of 6 laser beams located at the centre of a quadrupole magnetic field that is produced by a pair of coils in anti-Helmholtz configuration. During the 130 ms MOT stage, the cooling laser beams and quadrupole field trap an initial cloud of $\sim 10^8$ atoms. After the MOT quadrupole field is turned off, the atoms undergo a molasses cooling for 40 ms to allow eddy currents to dissipate prior to the atoms being launched.

To launch the atoms, the frequency of the "Up" ("Down") laser beam is shifted by $+5.0(-5.0)$ MHz to create a molasses moving vertically upward at 4.3 m s$^{-1}$. After 0.6 ms, a final polarization-gradient cooling stage is performed in the moving molasses as the cooling beams are gradually extinguished over 1.3 ms while varying their detuning from $-13.5$ MHz to $-66.5$ MHz with respect to $f_{45}$. This results in typical atomic temperatures of $\sim 1$ μK, with the atom population distributed across the $|F = 4, m_F\rangle$ Zeeman states.

Shortly after launch, the atoms traverse a retro-reflected beam consisting of optical pumping light tuned to $f_{44}$ and repump light tuned to the $f_{34}$ transition. A small magnetic field is pulsed on during this time to ensure that the optical pumping light has π polarization to pump atoms into the $|F = 4, m_F = 0\rangle$ magnetic sublevel. Although it is possible to populate the $|F = 4, m_F = 0\rangle$ state with > 95% efficiency, the optical pumping process also heats the atomic cloud, reducing the detected signal. The optimal optical pumping power, therefore, achieves efficient state transfer while causing minimal heating. In NRC-FCs2, the optical pumping stage transfers $\sim 70\%$ of the atoms to the $|F = 4, m_F = 0\rangle$ state, while

increasing the effective atomic temperature to $\sim 2.0$ μK. This results in a four-fold increase in the detected signal.

A state selection process is used prior to the Ramsey interaction to initialize the atoms in a single clock state. Atoms in the state selection cavity experience the $\sim 125$ nT C-field, which splits the magnetic sublevels. As the atomic cloud passes through the state selection cavity, atoms in the $|F = 4, m_F = 0\rangle$ state are transferred to the $|F = 3, m_F = 0\rangle$ state by the resonant microwaves. The remaining atoms in the $|F = 4\rangle$ state are removed using an optical pusher pulse resonant with $f_{45}$ while the atoms traverse between the state selection and Ramsey microwave cavities. This pusher light is generated by pulsing on the "Up" cooling beam to provide light with an intensity of 1 mW cm$^{-2}$ for a duration of 2 ms, 15 ms before the atoms enter the Ramsey cavity.

After the state selection process, the atoms pass upwards through the Ramsey cavity, where they experience a π/2 microwave pulse. The atoms continue their ballistic flight upwards and reach an apogee 27.6 cm above the centre of the Ramsey cavity, resulting in a Ramsey time of 478 ms. On their descent, the atoms experience a second π/2 microwave interaction in the Ramsey cavity before falling into the state detection region.

In the state detection region the relative population in each clock state is determined by measuring the fluorescence with two photodiodes as previously described. The number of atoms $N_4$ ($N_3$) is determined by the total fluorescence collected in the upper (lower) detection regions. The ratio $S \equiv N_4/(N_3 + N_4)$ is a normalized measurement of the $|F = 3\rangle \leftrightarrow |F = 4\rangle$ transition probability, with reduced sensitivity to atom number fluctuations. In clock operation, the Ramsey microwave frequency is toggled between $\approx f_0 + 0.5$ Hz and $\approx f_0 - 0.5$ Hz. This measures the transition probability at approximately a half-width-at-half-maximum detuning below $(S_-)$ and above $(S_+)$ the central Ramsey fringe. The difference in transition probability is used to generate a correction to the microwave synthesizer frequency, $\Delta f = G(S_+ - S_-)$, where G is a servo loop gain. A correction is applied to the Ramsey microwave frequency via the DDS after every second fountain cycle.

## 3. Systematic biases

Many physical effects in a fountain can cause systematic biases in the measured caesium clock transition frequency. Here, we describe the evaluation of frequency biases of NRC-FCs2 and their uncertainties. All frequency biases are given as fractional values with 1 σ stated uncertainties.

### 3.1. Second order zeeman shift

A stable and uniform C-field is required in the Ramsey cavity and drift region to lift the degeneracy of the $m_F$ magnetic sublevels and to shift transitions involving the $m_F \neq 0$ states far off-resonance. Although the $|F = 3, m_F = 0\rangle \rightarrow |F = 4, m_F = 0\rangle$ clock transition is insensitive to a first-order Zeeman shift, it does experience a second-order Zeeman shift,
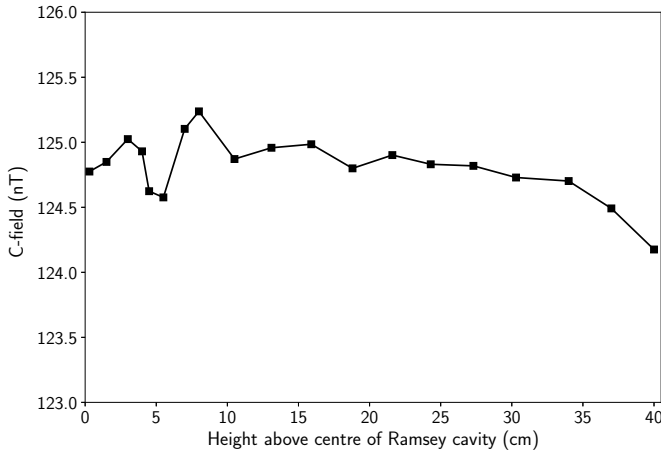
**Figure 4.** C-field map of the drift region. The typical launch apogee is 27.6 cm above the centre of the Ramsey cavity.

which is the largest corrected shift of NRC-FCs2. The frequency shift of an atomic state due to a static magnetic field can be calculated using the Breit-Rabi formula [19]; for the $^{133}$Cs clock transition, the frequency shift in Hz is given by [20]

$$\Delta f = 427.45 \times 10^8 B_0^2,\qquad(1)$$

where $B_0$ is the magnetic field in T.

In an atomic fountain, atoms are not stationary during their Ramsey interrogation time. Therefore, to evaluate the magnetic field-induced frequency shift, it is necessary to map the C-field over the trajectory of the atoms. In NRC-FCs2, this was done by measuring the frequency of the magnetically-sensitive $|F = 3, m_F = -1\rangle \rightarrow |F = 4, m_F = -1\rangle$ transition, while varying the launch height with ~0.5 cm resolution. At each height, the measured frequency is proportional to the time-averaged magnetic field sampled by the atoms between passages through the Ramsey cavity, $\langle B \rangle$. By launching to different heights, it is possible to construct a map of the magnetic field in the drift region, as shown in figure 4.

In normal operation, atoms are launched to an apogee of 27.6 cm above the centre of the Ramsey cavity. Over this trajectory, the C-field is homogeneous to ~200 pT, which corresponds to a field uniformity of ~0.2%. The C-field begins to vary more significantly near the top end of the C-field solenoid, which is 53 cm above the centre of the Ramsey cavity.

The measured clock frequency is sensitive to the time-average of the squared magnetic field, $\langle B^2 \rangle$, sampled by the atoms during their free-flight between Ramsey interactions. Therefore, using a single measurement of the linear time-averaged C-field, $\langle B \rangle$, leads to an uncertainty in the evaluation of the frequency bias, due to the variance of the field along the vertical axis, $\langle B^2 \rangle - \langle B \rangle^2$. However, as the C-field of NRC-FCs2 is uniform to 0.2% over the ballistic trajectory of the atoms, the spatial variance contributes a negligibly-small uncertainty of $< 10^{-18}$, and perfect homogeneity is assumed for frequency shift calculations.
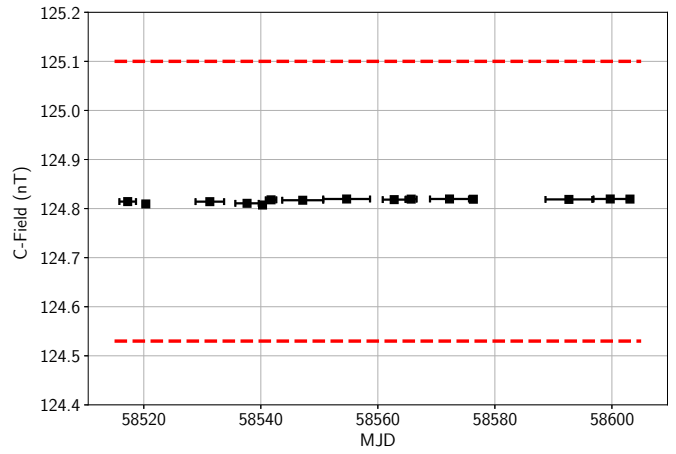


**Figure 5.** Time-averaged C-field. The horizontal error bars denote the duration of each measurement and the vertical error bars are < 0.002 nT and are smaller than the data points. The dashed red lines indicate the positions of the two adjacent Ramsey fringes.

The uncertainty of the frequency bias is limited by the long-term temporal stability of the C-field. This is measured regularly in the standard clock protocol by locking the local oscillator to the central Ramsey fringe of the $|F = 3, m_F = -1\rangle \rightarrow |F = 4, m_F = -1\rangle$ transition, $f_{3,-1\rightarrow4,-1}$, for the standard launch height. As shown in figure 5, the C-field derived from measurements of $f_{3,-1\rightarrow4,-1}$ shows excellent stability with variations far below the ~0.3 nT separation between Ramsey fringes, indicated by the dashed red lines. As the central Ramsey fringe of the magnetically sensitive transition can be tracked unambiguously, measurements of the time-averaged field at the full launch height are sufficient for characterizing the C-field, and full spatial mapping is only repeated intermittently.

The time-averaged C-field sampled by the atoms for our typical launch height has been measured to be $124.83 \pm 0.02$ nT for the data shown in figure 5. Using equation (1), we obtain a frequency shift of the clock transition in NRC-FCs2 of $724.6(2) \times 10^{-16}$.

### 3.2. Blackbody radiation (BBR) shift

The atoms in free flight between Ramsey interrogations are perturbed by the thermal radiation of their enclosure. If one assumes that the drift tube is well approximated as a blackbody radiator, the associated fractional frequency shift is given as

$$\frac{f}{f_0} = \beta \left( \frac{T}{300\ \text{K}} \right)^4 \left[ 1 + \epsilon \left( \frac{T}{300\ \text{K}} \right)^2 \right],\qquad(2)$$

where $T$ is the temperature of the drift tube [21]. We use the numerical values $\beta = -1.710(6) \times 10^{-14}$ and $\varepsilon = 1.3(1) \times 10^{-2}$ as calculated in [22, 23] respectively.

The temperature is monitored with three T-type thermocouples placed along the length of the water cooling jacket. The thermocouples and readout system have been calibrated to an accuracy better than 0.1 K. The variation in temperature between the sensors is less than 0.1 K, and the temporal
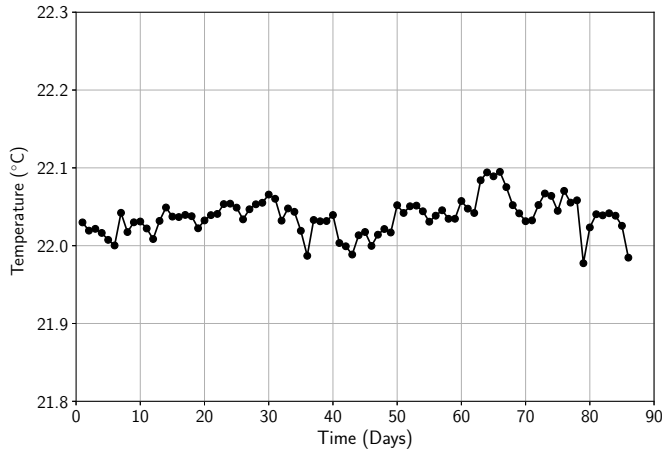
**Figure 6.** Temperature record of the flight jacket. Data points are the combined one-day averages of the three thermocouples along the drift tube.



**Figure 7.** Collisional shift measured in NRC-FCs2 for typical low atom density. Here the cloud has temperature $T = 2.0$ μK (after optical pumping) and initial radius $w = 1.2$ mm.

drift of the temperature is less than 0.1 K over several months, as shown in figure 6. Taking a combined overall temperature uncertainty as 0.2 K, the frequency bias in NRC-FCs2 due to BBR is $-162.3(7) \times 10^{-16}$.

### 3.3. Collisional shift

The frequency shift due to collisions between cold atoms is commonly one of the most significant sources of uncertainty in fountain clocks. Caesium has a particularly large collisional cross-section at low temperatures compared to other alkali atoms such as rubidium, which has a collisional cross-section approximately 30 times lower [24–26]. Experimentally, the collisional shift can also be challenging to minimize, as fountain clocks require a high atom number to suppress quantum projection noise (QPN). Some fountains reduce the shift by working with dilute clouds of atoms loaded directly from an optical molasses [6–10, 27, 28], however, the total detected atom number is then reduced. For fountains operating with a MOT stage, such as NRC-FCs2, care must be taken to accurately measure and correct the collisional shift.

A method for minimizing the collisional shift was previously developed in [29]. This method utilizes the difference in collisional rate coefficients of the two clock states. For low collisional energies, the collisional rate coefficients for $|F = 3\rangle$ and $|F = 4\rangle$ have opposite sign. Therefore, by manipulating the state composition after the first Ramsey interaction, $\rho_{40} \equiv \frac{N_4}{N_3 + N_4}$, it is possible to cancel the collisional shift. This is done by adjusting the pulse area of the first Ramsey interaction. Additionally, this method relies on low collisional energies, which can be effectively tuned by varying the initial size and temperature of the atomic cloud.

Fountain clocks typically apply a $\pi/2$ pulse during the Ramsey interactions, which results in $\rho_{40} = 0.5$. This maximizes the amplitude of the Ramsey fringes and, consequently, the signal-to-noise ratio. It was found that to cancel the collisional shift near $\rho_{40} = 0.5$ in NRC-FCs2, it was necessary to reduce the initial size and temperature of the atomic cloud. The atomic
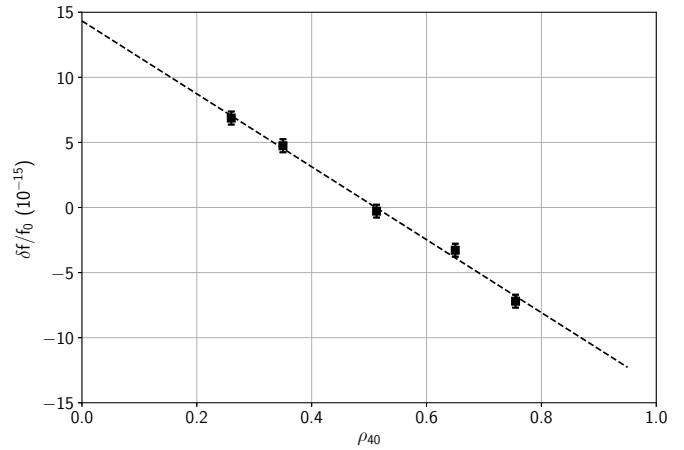
cloud temperature was minimized by optimizing laser alignment, background magnetic field cancellation, and laser frequency and amplitude ramp times. The cloud size was reduced by eliminating any extraneous expansion time in the experimental sequence, and by decreasing the MOT loading time. This resulted in a 1/$e$ atomic cloud radius of 1.2 mm and temperature of 2.0 μK.

To measure the magnitude of the collisional shift, the fountain was toggled between high and low density by varying the power of the state selection microwave pulse. Extrapolating to zero density gives a collisional shift-corrected frequency of

$$f_c = \frac{k f_L - f_H}{k - 1}, \tag{3}$$

where $f_H$ and $f_L$ are the measured clock frequencies at high and low densities, respectively, $k \equiv N_H/N_L$ is the ratio of high to low atom number, and $f_c$ is the frequency corrected to zero density.

The values for $k$ and the duty cycle ratio are chosen to maximize the short term stability of $f_c$ [30]. NRC-FCs2 typically operates with $k \sim 7$–8, and is alternated between high and low density with a duty cycle of approximately 1 to 8.

Figure 7 shows the collisional shift for typical low atomic density as the pulse area of the first Ramsey interaction was varied. Here, the collisional shift, $\delta f = f_L - f_c$, is plotted in fractional frequency. It can be seen that the collisional shift in NRC-FCs2 is canceled for $\rho_{40} \simeq 0.5$, corresponding to $\pi/2$ Ramsey excitation. Though this technique helps reduce the effect of the collisional shift dramatically, the size and temperature of the cloud vary in time and, therefore, it is still necessary to continually measure the effect of cold collisions.

In practice, the measured signal is proportional to the atom number and not the atomic density. If the spatial profile of the cloud changes between high and low atom numbers, it would result in an error in the ratio, $k$. This could occur, for example, due to variations in the microwave field amplitude across the atomic sample in the state selection cavity. To investigate this, we have compared the Time-of-Flight (ToF) profiles for low
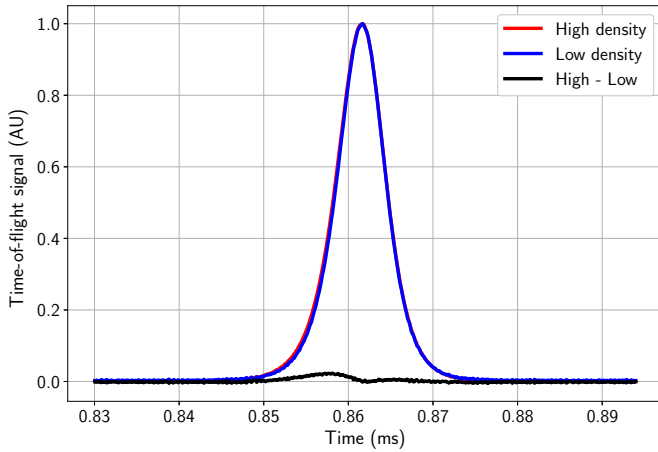
**Figure 8.** Normalized time-of-flight signals measured on the atoms' descent. The black line is the difference between the normalized signals for high and low atomic density with $k = 7$.

and high atom number as shown in figure 8. The difference between the normalized ToF signals (high-low) for the downward passage of the atoms through the detection region is shown by the black curve and is less than 2%. As we use the state selection microwaves to vary the atom number, we are unable to compare the profiles of the low and high density atom clouds on the upward transit of the detection region where any initial difference in density profile might be more obvious. As such, we take a 10% uncertainty in $k$ as a conservative upper bound. For typical values for collisional shift and $k$, this yields an uncertainty of $1 \times 10^{-16}$ as the collisional shift for low density is typically maintained below $1 \times 10^{-15}$.

### 3.4. AC stark shift

The electromagnetic field from background light can shift the energy levels of the clock transition, causing a frequency bias. To avoid this, care is taken to extinguish the laser light in the physics package during the ballistic flight of the atoms between microwave interactions. In addition to mechanical shutters, the cooling and detection light are also extinguished by switching off the RF power driving the AOMs. To verify that the shutters are functioning properly, the fountain was toggled between normal operation and a protocol where the cooling beam and detection AOMs are on during the ballistic flight of the atoms and the light is extinguished only with the mechanical shutters. No shift was found to a fractional uncertainty of $5 \times 10^{-15}$. The AOMs provide over 50 dB of attenuation, rendering any light shifts $< 10^{-19}$.

In the standard experimental sequence, the most likely source of leakage light is the pusher pulse. This is because the pusher pulse is applied shortly ($\sim 15$ ms) before the first Ramsey interaction, and it is generated by a vertical cooling beam, which can directly illuminate the atoms during their ballistic flight. Care must be taken in the timing of the mechanical shutters. We therefore have two optical shutters for redundancy and check the shutter timings intermittently.

The repump and optical pumping light are switched off only with mechanical shutters. To ensure the shutters were sufficient, we toggled the fountain between normal operation and a sequence in which the shutters for optical pumping light and repump light (used during the MOT, optical pumping, and detection stages) were left open. A light shift of $9(2) \times 10^{-15}$ was measured, but as all shutters were confirmed to provide $> 50$ dB of attenuation (limited by the measurement), any possible light shift during normal operation is below a fractional uncertainty of $10^{-19}$, and is therefore negligible.

### 3.5. Background gas

It is expected that the background pressure is predominantly due to Cs flowing from the reservoir into the MOT chamber and hydrogen outgassing from the metal surfaces within the vacuum system. The effect of background gas collisions can be quantified through measurements of the loss of cold atoms during the Ramsey time, as shown in [31]. There, it was found that the fractional frequency shift due to collisions with background Cs atoms is given by $f/f_0 < 2 \times 10^{-16} \Delta A$ for a Ramsey interaction time of 0.5 s, where $\Delta A$ is the fractional loss of atoms from the cold atom cloud. Though the majority of the fractional loss is due to clipping of the atomic cloud on the system apertures during its descent, it is possible to make relative measurements of the atom loss as a function of Cs background pressure.

To measure frequency bias of NRC-FCs2 due to collisions with background Cs atoms, we varied the background Cs pressure by adjusting a valve between the Cs reservoir and the MOT chamber and varying the temperature of the Cs reservoir. Relative changes in the Cs background pressure were monitored via measurements of the background fluorescence in the detection region using resonant light. It was found that increasing the Cs background pressure by a factor of three resulted in a change in fractional loss of atoms of $< 4\%$. We, therefore, conclude that our fractional loss under normal conditions is $\Delta A < 0.02$. The predicted bias is then calculated to be $< 4 \times 10^{-18}$.

To determine the effect of background $H_2$, we use the background pressure measured from the current of the three ion pumps; which ranges from $4 \times 10^{-11}$ to $3 \times 10^{-10}$ mbar. We use the highest pressure reading as a conservative upper bound, and assume that the background gas is purely $H_2$. Using the pressure shift coefficients calculated in [31], the relative frequency shift due to background collisions with $H_2$ is calculated to be $< 4 \times 10^{-18}$. Combining the contributions from $H_2$ and Cs yields a shift $< 8 \times 10^{-18}$. No frequency correction is applied to NRC-FCs2 for background gas collisions, however, $8 \times 10^{-18}$ is assigned as the uncertainty.

### 3.6. Distributed cavity phase (DCP) shift

The spatial variation of the microwave phase in the Ramsey cavity can lead to significant shifts of the clock's frequency. Non-uniform losses in the cavity walls or asymmetrical feeding can create small, traveling-wave components of the microwave field. This results in spatial phase variations
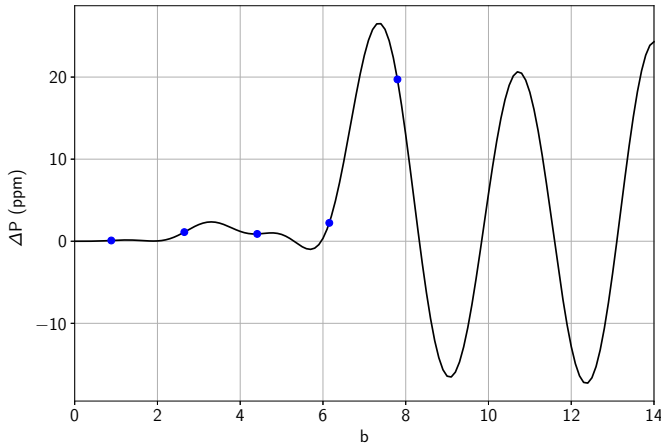
**Figure 9.** Calculated perturbations to the clock transition probability, $\Delta P$, due to the $m = 0$ component of the DCP. The field amplitude is b, with b $\sim$ 1 for $\pi/2$ pulse area. The blue circles denote 1, 3, 5, 7, and 9 $\times$ $\pi/2$ pulses.

throughout the cavity, which, when coupled with the transverse motion of the atomic cloud, lead to Doppler shifts of the measured frequency. This effect is known as the distributed cavity phase shift (DCP) and is a leading contribution to the error budget in many state-of-the-art fountain PFSs [5, 6, 9].

In [16, 32] the DCP is described by a Fourier expansion of the microwave field in a cylindrically symmetric cavity in terms of azimuthal modes, $g_m(r, z) \cos m\phi$, where $r$ and $z$ are the transverse radial and longitudinal coordinates, $m$ is an integer, and $\phi$ is the azimuthal angle. Because the atomic trajectory is close to the cavity axis where $g_m(r,z) \propto r^m$, only the lowest few modes ($m \leq 2$) cause a significant shift and each is treated separately below.

### 3.6.1. m = 0.

The $m = 0$ component represents azimuthally symmetric phase gradients that are predominantly along the cavity axis. These gradients typically cause frequency shifts that are small at low power, but can be significant at elevated microwave powers [33]. The cavity in NRC-FCs2 uses a cylindrically-symmetric geometry that is designed to minimize the $m = 0$ component of the DCP for moderate microwave amplitudes [17]. Figure 9 shows the predicted perturbation, $\Delta P$, to the transition probability at the positive detuning ($\approx f_0$ + 0.5 Hz) in clock mode, as a function of the microwave amplitude in the Ramsey cavity. The prediction is based on fields from finite-element modeling and a Monte Carlo simulation [5, 6, 9, 16]. The typical parameters of NRC-FCs2 are an rms atomic cloud size of 1.2 mm radius and temperature of 2.0 μK. A change in transition probability can be converted to a frequency bias, as $\Delta f = \Delta P / S'(f)$, where $S'(f)$ is the slope of the Ramsey fringe at the microwave frequency $f \approx f_0$ + 0.5 Hz. Assuming a potential difference in endcap surface resistances of 10%, the predicted frequency bias for NRC-FCs2 operating with $\pi/2$ Ramsey interrogation pulse area ($b \simeq 1$) is 0.07 (36) $\times 10^{-16}$.

### 3.6.2. m = 1.

The $m = 1$ component represents a linear transverse phase gradient near the centre of the cavity, for
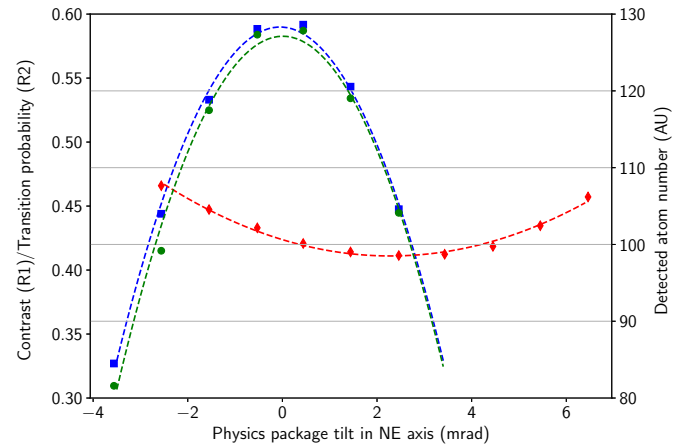


**Figure 10.** The blue squares represent the measured contrast of Rabi oscillations during the upward passage through the Ramsey cavity, R1. The detected atom number is shown by the green circles and the transition probability due to Rabi excitation during the downward passage through the Ramsey cavity, R2, is shown by the red diamonds.

example, from power flow across the cavity. It produces a frequency shift when combined with a displacement of the centre of mass of the atom cloud in the transverse plane of the cavity between the upward and downward passages. Here, a nonvertical launch will cause the atoms to have, on average, a nonzero transverse velocity. This causes a Doppler shift due to the traveling-wave component of the microwave field. If, however, the launch is vertical and on-axis with the Ramsey cavity, the $m = 1$ shift will be suppressed. Therefore, knowledge of the atomic trajectory and balancing the feeds to eliminate phase gradients are central to evaluate the $m = 1$ DCP frequency bias.

A nominal vertical alignment can be found using a number of methods. In many cases, the Ramsey cavity is fed from alternating directions, while tilting the fountain [5, 8, 33]. This is also done at several microwave powers and the tilt at which the frequency difference between feed directions is minimal is taken as true vertical. This is difficult in our fountain because the $m = 1$ DCP shift induced by the feeds in our clock cavity is small. We employed an alternative method that determines the position of the atomic cloud with respect to the Ramsey cavity axis during the upward and downward transits and optimizes the number of detected atoms.

To measure the position of the atoms during their ascent, we measure the contrast of Rabi oscillations at high microwave amplitudes with microwaves applied to the Ramsey cavity only during the atoms' upward flight, $R1$. Because the amplitude of the microwave field in the cavity varies spatially, the pulse area is proportional to as $J_0(2\pi f_0 r/c)$ [5], so the contrast of $R1$ will be maximized when the atoms are centred on the cavity's axis (blue squares in figure 10). We detect the transition probability, $S \equiv N_4/(N_3 + N_4)$, for $11\pi$ and $12\pi$ pulses, and take the difference as a measure of the contrast, which gives a large position sensitivity for a small cloud. To maximize the contrast, we translate the initial cloud position using auxiliary magnetic field shim coils mounted on the horizontal MOT viewports. The position of the cloud is also measured

using two triggered CCD cameras. We centre the ascending cloud while simultaneously maximizing the total detected atom number by tilting the fountain (green circles in figure 10). This essentially centres the cloud on the aperture below the state selection cavity in the below-cutoff waveguide, which blocks ∼80% of the atoms on their descent. This alignment of the fountain tilt and the initial cloud position is used for normal operation.

During the downward transit through the Ramsey cavity, the atoms can similarly be centred on the microwave cavity axis. Because the cloud is larger, the microwave field amplitude sampled by the individual atoms will vary more significantly than in the case of R1, and the contrast of the Rabi oscillations will decay more rapidly. Therefore, we achieve optimal sensitivity of the transition probability by applying lower amplitude $2.5\pi$ pulses during the atoms' descent, $R2$. We measure the transition probability, $S$, as a function of the fountain tilt angle. With an atom cloud traveling vertically on the fountain axis, the measured ratio has an extremum when the detected part of the atom cloud is centered on the microwave cavity axis (red diamonds in figure 10).

However, if the atoms' launch velocity is not parallel to the fountain axis, the tilt that minimizes $R2$ will not coincide with that which maximizes the number detected, because the aperture is 20.1 cm below the Ramsey cavity. We use the difference in tilt angle between maximum detected number and minimum R2 and our Monte Carlo model to determine the launch velocity transverse to the fountain axis. The measured tilt differences of $-2.42(14)$ mrad NE and $-3.42(16)$ mrad NW give velocities of $-13.0$ mm s$^{-1}$ and $-18.6$ mm s$^{-1}$. Here, this implies that the fountain is tilted at $-2.93$ mrad and $-4.36$ mrad, with initial offsets of 1.79(20) mm and 2.63(35) mm for normal operation. We note that, in general, this alignment procedure for normal operation, which varies initial position to maximize $R1$, does not necessarily yield a maximum of $R1$ versus fountain tilt at the angle that maximizes the number detected.

We use our finite-element model and Monte Carlo simulation to calculate the $m = 1$ frequency shift for normal operation, but with only a single cavity feed, and for the tilt that minimizes $R2$. These give the scale of the $m = 1$ DCP shift for normal operation and its sensitivity to fountain tilt. For example, the $m = 1$ DCP shift is 3.7 times smaller for normal operation than for the $-2.42$ mrad NE tilt at the minimum of $R2$ in figure 10. Thus, the fountain's tilt offset from vertical for normal operation is $-2.42/3.7 = -0.65$ mrad parallel and $-0.92$ mrad perpendicular to the microwave cavity feeds. To get the $m = 1$ DCP uncertainty, we take half of the angle biases as the uncertainties and multiply these by the tilt sensitivities for balanced feeds, including their uncertainties.

We measure the tilt sensitivity of the fountain clock's frequency operating at normal conditions (with balanced feeds) and alternating the tilt of the physics package by $\pm 2.5$ mrad ($\pm 4.5$ mrad) from vertical for the axis parallel (perpendicular) to the microwave feeds. The data is shown in figure 11. A larger range in tilt angle was used perpendicular to the feeds as that data was taken later, after we had improved the signal to noise such that we could operate at lower atom number without
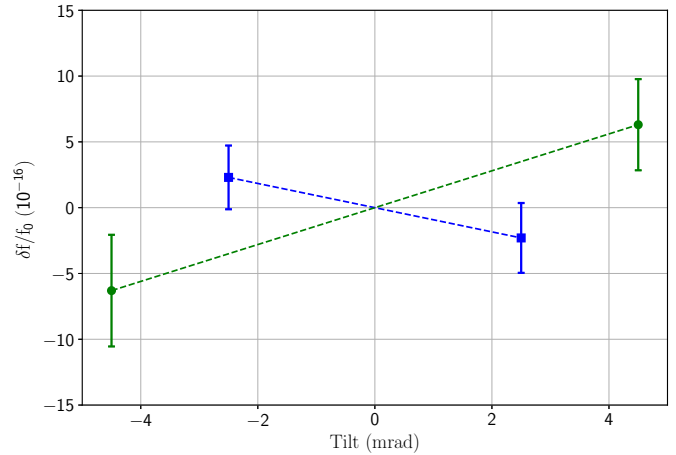


**Figure 11.** The blue squares (green circles) show the measured frequency vs tilt angle parallel (perpendicular) to the microwave feed axis. The data is taken with two balanced microwave feeds. The frequency at each tilt angle is plotted with respect to the average frequency.

significantly degrading the short term stability. The data were collected at each tilt for intervals of 12 hrs, alternating the order of the tilts to minimize the effect of maser drift. The difference between the measured frequencies for the alternating tilts gives sensitivities of $-0.9(8) \times 10^{-16}$ mrad$^{-1}$ and $1.4(5) \times 10^{-16}$ mrad$^{-1}$ parallel and perpendicular to the cavity feeds. Multiplying these by our tilt offset leads to an overall uncertainty of $1.3 \times 10^{-16}$ for the $m = 1$ component and we do not correct the frequency for the $m = 1$ DCP bias.

*3.6.3. m = 2.* We calculate the DCP frequency bias and its uncertainty due to $m = 2$ quadrupole phase variation of the Ramsey microwave field. Inhomogeneous detection of the atoms, particularly along the feed axis of the Ramsey microwaves, as well as an offset of the atomic cloud from the centre of the Ramsey cavity can lead to a $m = 2$ DCP shift. We use the above modeling of the positions of our atoms as in figure 10. In NRC-FCs2, the state detection light is uniform to 5%, and is at 45° to the microwave feed axis. We calculate a small frequency bias and uncertainty of $0.04(20) \times 10^{-16}$.

### 3.7. Microwave lensing

Fountain clocks are sensitive to another bias from the microwave field, known as "microwave lensing". Unlike the DCP shift, it is caused by the standing-wave component of the microwave field. When atoms traverse a standing wave near its antinode, their wavefunctions undergo a lensing effect due to the curvature of the amplitude of the field [34]. The dipole forces during the first Ramsey interaction act as positive or negative lenses on the two dressed states of the atom. The second Ramsey interaction transfers the focused dressed state into the upper hyperfine state for the positive detuning ($\approx f_0 + 0.5$ Hz) in clock mode, and likewise transfers the defocused state into the upper hyperfine state for the negative clock

detuning [5, 6, 9, 34]. This yields a positive bias of the clock's frequency.

The effect of microwave lensing in NRC-FCs2 is modeled following the treatment in [9, 34]. In NRC-FCs2, the detection light is homogeneous within 5%, the initial atom cloud width is 1.2 mm, and the atomic temperature is 2.0 μK. For these parameters we obtain the microwave lensing frequency bias in NRC-FCs2 to be $0.6(2) \times 10^{-16}$, which is corrected.

### 3.8. Microwave leakage

In an ideal fountain clock, atoms interact with resonant microwaves only while inside the microwave cavities. In reality, there will be weak interactions due to microwave leakage above and/or below the Ramsey cavity. The physics package of NRC-FCs2 has been designed to minimize the effect of such leakage by including a 40 cm long below-cutoff waveguide above the Ramsey cavity that attenuates any stray microwaves by 0.6 dB mm$^{-1}$. This results in an attenuation of external microwaves of > 70 dB at the apogee of our typical launch.

Therefore, we consider only the effect of additional microwave interactions occurring below the Ramsey cavity. On the atoms' ascent, the state selection process transfers atoms into the $|F = 3, m_F = 0\rangle$ state before the pusher beam removes the remaining $F = 4$ atoms. This occurs while the atoms are in a below-cutoff microwave waveguide between the state selection and Ramsey cavities. At this point, the atoms have been prepared in a pure clock state and the effect of any prior exposure to microwave leakage is eliminated. Therefore, we are only sensitive to microwave leakage occurring below the Ramsey cavity during the atoms' descent, where the atoms are not shielded from background microwaves. For this situation, the effect on the transition probability between clock states is given by [35–37]

$$\Delta P = 2A\theta_1 \sin 2\pi \delta T \sin \theta_1, \qquad (4)$$

where $\Delta P$ is the perturbation to the $|F = 3\rangle \rightarrow |F = 4\rangle$ clock transition probability, $\delta$ is the detuning of the microwaves from the atomic resonance, $T$ is the Ramsey time, $\theta_1$ is the pulse area of the first Ramsey interaction, and $A$ is a scaling factor dependent on the amplitude and the phase of the microwave leakage field. Here, it is assumed that the field amplitude of the leakage microwaves scales linearly with the applied Ramsey microwave amplitude. Also, equation (4) represents the effect of the out-of-phase component of the leakage microwave field with respect to the applied Ramsey microwave field, as leakage microwaves in-phase with the Ramsey field do not produce a shift in the clock frequency.

To eliminate the possibility of leakage below the Ramsey cavity, a frequency shift key (FSK) function in the microwave synthesizer was used which rapidly detunes the frequency to be 1 MHz off resonance after the atoms fall through the Ramsey cavity. To investigate the effects of microwave leakage in NRC-FCs2, the fountain was run at elevated Ramsey microwave amplitude both with and without using the FSK function.
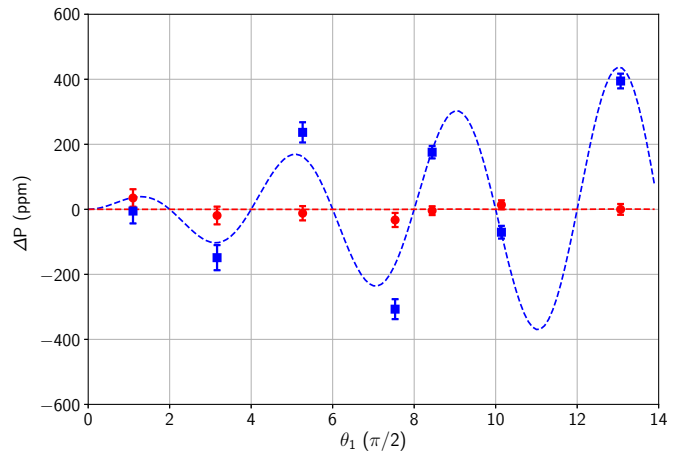


**Figure 12.** Perturbations of the clock transition probability, $\Delta P$, as a function of Ramsey interaction pulse area. Blue squares represent a differential measurement with/without FSK. The red circles represent data taken with FSK.

In figure 12, the blue squares represent a differential measurement where the frequency difference measured with/without using FSK was converted to the change in transition probability, $\Delta P$. $\Delta P$ is calculated by multiplying the measured difference in clock frequency with the slope of the central Ramsey fringe at the lock point with positive detuning ($\approx f_0 + 0.5$ Hz). The red circles represent data taken with FSK, where $\Delta P$ is calculated from the deviation of each measured frequency from the mean of all FSK measurements. The predicted $m = 0$ contribution has also been subtracted from this data, but has a negligible effect within the uncertainty of the measurements. As can be seen, there is an obvious effect of microwave leakage on the transition probability, which FSK strongly suppresses. The dashed lines show fits using equation (4) with only $A$ as a free parameter. We observe excellent agreement between the model and the experimental data for both with and without FSK. From the model, we determine a shift in fractional frequency of $35(4) \times 10^{-16}$ due to microwave leakage for typical parameters ($\pi/2$ Ramsey pulse area), which FSK reduces to $0.1(1.0) \times 10^{-16}$ with the use of FSK.

### 3.9. Microwave generation and spectrum

Typically, the 9.2 GHz microwaves used for Ramsey interrogation are synthesized using a high stability quartz crystal oscillator that generates a signal in the RF spectrum (5 MHz or 10 MHz). The synthesis chain creates some unwanted harmonics in the final microwave spectrum, and amplifies spurious spectral components present in the 5 MHz reference signal from the quartz crystal. Asymmetries in the microwave spectrum with respect to the caesium resonance frequency can cause a frequency bias [38].

In NRC-FCs2, the microwave spectrum is generated by locking an SDI CS-1 microwave synthesizer to the 5 MHz signal from an active hydrogen maser (Vremya-CH). We have examined the spectrum and found that all spurious harmonics
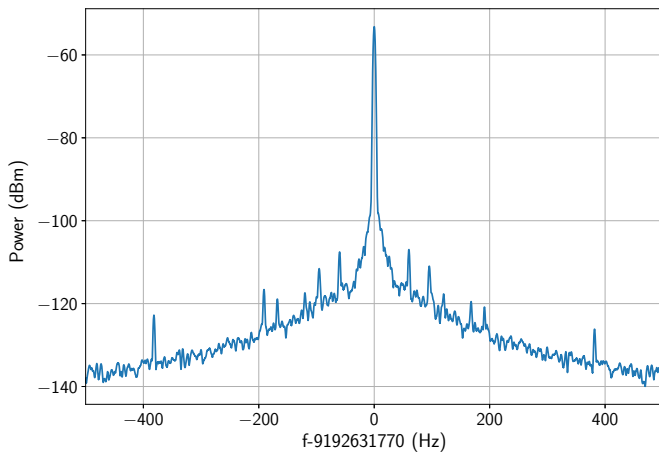
**Figure 13.** RF spectrum of the synthesized microwaves used for Ramsey interrogation.

are dramatically suppressed from the carrier frequency. As shown in figure 13, the largest harmonics are generated by the line frequency and occur at $\pm 60$ Hz but are 55 dB below the carrier frequency power and are symmetric to within $\sim 10\%$. There are also spurious spectral components occurring near $\pm 95, \pm 120, \pm 168, \pm 191,$ and $\pm 380$ Hz, but the spectral power of these components decreases with detuning from the carrier frequency and they have a negligible contribution. Using the treatment in [39] yields a relative frequency bias of $< 1 \times 10^{-17}$ and we, therefore, neglect this effect.

### 3.10. Rabi and ramsey pulling, and Majorana transitions

Rabi pulling is a frequency bias that arises primarily from the tails of the Rabi pedestal of the $|F = 4, m_F = \pm 1\rangle \leftrightarrow |F = 3, m_F = \pm 1\rangle$ transitions, whereas Ramsey pulling is caused by $\sigma$ transitions from $m_F = \pm 1$ states into the $m_F = 0$ clock states. Therefore, both shifts are caused by an asymmetry in the populations of the $m_F = \pm 1$ states. In thermal beam clocks these effects could cause signifcant frequency biases due to the presence of atoms in $m_F \neq 0$ states, however, in atomic fountain clocks these effects are strongly suppressed due to the state selection process, where atoms in the $m_F \neq 0$ states are removed. In NRC-FCs2, we have measured the fraction of atoms in the $m_F = \pm 1$ states to be less than $10^{-3}$, with asymmetry below $5 \times 10^{-4}$. Following the treatment in [40], we calculate shifts for Rabi and Ramsey pulling to both be well below $10^{-17}$ in fractional frequency. We do not correct for these shifts.

Majorana transitions can occur when an atom experiences a magnetic field which varies rapidly compared to its Larmor precession frequency, such as near a magnetic zero crossing. This can result in transitions between Zeeman sublevels as the atomic dipole cannot follow the field adiabatically. It has been shown that this effect can cause shifts in atomic fountain clocks when there is an asymmetric distribution among the Zeeman sublevels [41]. In NRC-FCs2 we have a very small ($< 5 \times 10^{-4}$) fractional imbalance in $m_F$ populations after our

state selection process. To avoid Majorana transitions occurring over the 20 cm between the magnetically shielded region and the detection zone, we have added a small ( 0.1 G) auxiliary magnetic field from a "guide" coil located just below the magnetic shields. The coil ensures that the magnetic field varies smoothly and has no zero crossings along the trajectory of the atoms.

### 3.11. Cavity pulling

Though cavity pulling effects were significant contributions to the frequency uncertainty of thermal beam clocks, they are drastically reduced in fountain clocks. First-order cavity pulling is due to the maser action of the atoms in the microwave cavity and is proportional to the atomic density in the cavity. In NRC-FCs2, this effect is small for the typical atom number and it is continuously corrected, along with the effects of cold collisions, by toggling the atomic density from high to low and extrapolating to zero density.

When the cavity resonance is not tuned to the atomic resonance, the microwave amplitude will vary asymmetrically with positive/negative detunings from the atomic transition frequency. Since our measurement involves a square-wave frequency modulation centred on the caesium resonance, this effect can result in a frequency bias and is known as second order cavity pulling. It is calculated based on the theoretical treatment in [20]. The temperature servo for the drift tube keeps the Ramsey cavity tuned within 30 kHz of the clock frequency and the Ramsey microwave interrogation pulse area is within 10% of a $\pi/2$ pulse. We find that these parameters give a shift below $1 \times 10^{-17}$ in fractional frequency. Consequently, we neglect this effect.

### 3.12. Synchronous phase transients

Small phase variations in the synthesized microwaves between Ramsey interactions can have a significant impact on the accuracy of a fountain clock. A phase difference of even 3 μ rad will cause a bias of $\sim 1 \times 10^{-16}$ in fractional frequency. Although random variations will average out, phase transients that are synchronized with the experimental cycle can cause a measurement bias.

This effect can be difficult to characterize experimentally. It is possible, though challenging, to directly measure the phase of the synthesized microwaves at the $\sim 10^{-16}$ level [42] with a transient-free microwave reference. The likely cause of synchronous phase transients is any equipment that has a transient behavior synchronized with the experimental cycle.

In NRC-FCs2, we use an FSK function to detune the Ramsey microwaves, effectively functioning as a microwave switch. As the FSK function is used in synch with the experimental cycle, it could potentially cause an induced phase transient in the synthesizer. However, as the FSK function only varies the frequency of the microwaves (and not power), there should be minimal induced phase transients. We evaluated the frequency shift due to the FSK function by varying the timing of the FSK pulse to switch the microwaves back to resonance shortly before the atoms' upward passage through the state

selection cavity (∼60 ms before the first Ramsey interaction). In this case, no frequency shift was measured within the measurement uncertainty of $5 \times 10^{-16}$. In practice, we only use the FSK function to detune the microwaves after the second Ramsey interaction, switching the synthesizer back on resonance nearly 400 ms before the first Ramsey interaction in the next experimental cycle. This leaves a significant amount of time for phase transients to dissipate. We believe that there is more than a factor of 10 suppression of any phase transients for the typical timing [42], which gives an upper bound of $5 \times 10^{-17}$ for the frequency uncertainty due to FSK-induced phase transients.

AOM RF amplifiers and optical shutters are also potential causes of synchronous phase transients via emitted EM radiation. In particular, pulses occurring during, or just before, a Ramsey interaction time are the most likely to cause a significant bias. In normal operation, the AOM and shutter switch ∼15 ms before the atoms enter the Ramsey cavity to provide a pusher pulse after the state selection process, and are the most likely elements to cause a significant phase transient. To investigate this effect, the system was run alternating between the standard clock protocol and a configuration where a shutter was opened and an RF amplifier was powered during the first Ramsey interaction time. No difference was observed within the measurement uncertainty of $3 \times 10^{-16}$. We believe that the sensitivity for pulses occurring during the Ramsey interaction is more than a factor of 5 higher than for our typical timing, and consequently we use $6 \times 10^{-17}$ as the uncertainty in the phase transient-induced frequency shift caused by optical shutters and AOM amplifiers. Combining this with the FSK-induced contribution, we obtain $8 \times 10^{-17}$ as the uncertainty of the frequency bias due to microwave phase transients; no correction is applied.

### 3.13. Gravity

Although caesium fountain clocks measure proper time, we wish to compare NRC-FCs2 with other timescales and to contribute to TAI. This requires that NRC-FCs2 be measured against other clocks located at differing gravitational potentials that, consequently, experience unequal gravitational redshifts. Therefore, we determine the frequency bias of NRC-FCs2 with respect to operation on the geoid. Accurate knowledge is required of both local gravity and the orthometric height of the fountain clock, as the relative shift in frequency from operation on the geoid is given by [20]

$$\frac{\Delta f}{f_0} = \frac{gh}{c^2}, \quad (5)$$

where $g$ is local gravity, $h$ is the time-averaged orthometric height of the atoms, and $c$ is the speed of light.

The orthometric height of the laboratory has been determined through geodesic surveying performed by Natural Resources Canada [43]. Accounting for the 3.2 mm/yr vertical speed of the laboratory, the height of the atoms time-averaged over the ballistic flight between Ramsey microwave interactions is 95.797(24) m with respect to the geoid. It should
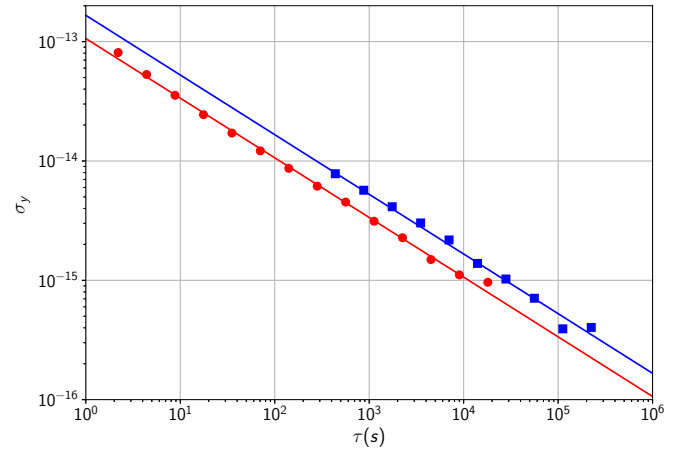


**Figure 14.** Overlapping Allan deviation of FCs2 for high atomic density, $f_H$, represented by the red circles and the collisional shift-corrected frequency, $f_c$, represented by the blue squares.

also be noted that although solid earth tides can cause variations in the gravitational redshift at the National Research Council Canada at the level of $\pm 2 \times 10^{-17}$, this is dominated by semi-diurnal effects which average down below $10^{-18}$ in under two days and can, therefore, be neglected. Local gravity at the National Research Council Canada has been surveyed and measured to be 9.80616(1) m s$^{-2}$. Using equation (5), we determine the frequency bias due to the gravitational redshift to be $104.52(3) \times 10^{-16}$.

### 3.14. Total uncertainty

The uncertainty budget for NRC-FCs2 is shown in table 1. The total systematic uncertainty is $2.3 \times 10^{-16}$, where cold collisions, microwave leakage and DCP give the largest contributions.

## 4. Performance of NRC-FCs2

### 4.1. Short term stability

NRC-FCs2 typically operates with a signal-to-noise ratio (SNR) of 1500–2000, which is not limited by quantum projection noise. We typically achieve a short term stability of $\sigma_y = 1.1 \times 10^{-13} \tau^{-\frac{1}{2}}$ at high atomic density, which is limited by the stability of the microwave local oscillator. This is degraded slightly to $\sigma_y = 1.2 \times 10^{-13} \tau^{-\frac{1}{2}}$ when running at the typical low density. When operating in normal clock mode, NRC-FCs2 is run at low density for 80%–90% of the time, toggling to high density for the remaining time (excluding < 1% used for C-field measurements). Extrapolating to zero density gives the collisional shift-corrected frequency, $f_c$, which shows a short term stability of $\sigma_y = 1.7 \times 10^{-13} \tau^{-\frac{1}{2}}$, as shown in figure 14. The short term stability of $f_c$ is in agreement with predictions based on equation (3) and the measured short term stability for our low and high densities.

**Table 1.** Uncertainty budget of NRC-FCs2 listing the systematic effects, as well as the associated frequency biases and uncertainties, given in parts in $10^{16}$. Effects with frequency biases and associated uncertainties $< 10^{-17}$ are neglected.

| Effect | Bias | Uncertainty |
|---|---|---|
| Zeeman Effect | 724.6 | 0.2 |
| Blackbody radiation | −162.3 | 0.7 |
| Gravitational redshift | 104.52 | 0.03 |
| Cold collisions[a] | 10 | 1 |
| Microwave leakage | 0.1 | 1.0 |
| Synchronous phase transients | – | 0.8 |
| DCP m=0 | 0.07 | 0.36 |
| DCP m=1 | – | 1.3 |
| DCP m=2 | – | 0.2 |
| Microwave Lensing | 0.6 | 0.2 |
| Total | 677.6 | 2.3 |

[a]A typical value for normal operation.

### 4.2. Frequency comparison

Since August 2018, the frequency of NRC-FCs2 has been compared to the SI second via a GPS link using the VM1 maser as a transfer oscillator. The frequency of VM1 was measured against NRC-FCs2 intermittently with uninterrupted measurements of up to 18-day duration. The phase difference between VM1 and UTC(NRC) was measured continuously to provide access to UTC/TAI and the SI second through the monthly Circular T reports, published by the BIPM.

The fractional frequency measurements of VM1 against NRC-FCs2, y(FCs2-VM1), were grouped by the Circular T publication period, typically 30 days [44], and corrected for the systematic shifts in table 1. We fit the y(FCs2-VM1) data to find the frequency difference of each circular T period at its midpoint, $y_m$(FCs2-VM1). The frequency measurement data were averaged for 2-hour intervals and the uncertainty of each data point was calculated using the Allan deviation. The VM1 frequency drift function was calculated from the frequency comparison of VM1 to TAI. This function was then used to fit y(FCs2-VM1) data using a weighted linear regression. The statistical uncertainty of y(FCs2-VM1) for the given measurement period was then used as the type-A uncertainty, $u_A$.

The link uncertainty between NRC-FCs2 and VM1, $u_{l/\text{Lab}}$, is the quadratic sum of two terms. The first term represents the phase fluctuation caused by the cables from VM1 to the fountain, which was estimated to be no larger than $1 \times 10^{-16}$. The second uncertainty is due to the dead time between fountain measurements [45] and was estimated using a numerical simulation of the measurement noise [46–48]. For frequency measurements between NRC-FCs2 and VM1, the noise characteristics were modeled as the quadratic sum of white FM and flicker FM, with contributions of $1.7 \times 10^{-13}\tau^{-\frac{1}{2}}$ and $4 \times 10^{-16}$, respectively. The estimated contribution of white FM noise was extracted from the Allan deviation of NRC-FCs2 while operating in normal clock-mode. The value of the flicker FM noise was a conservative estimate [49]. One hundred simulated frequency noise data sets were generated for each measurement period using the software Stable32
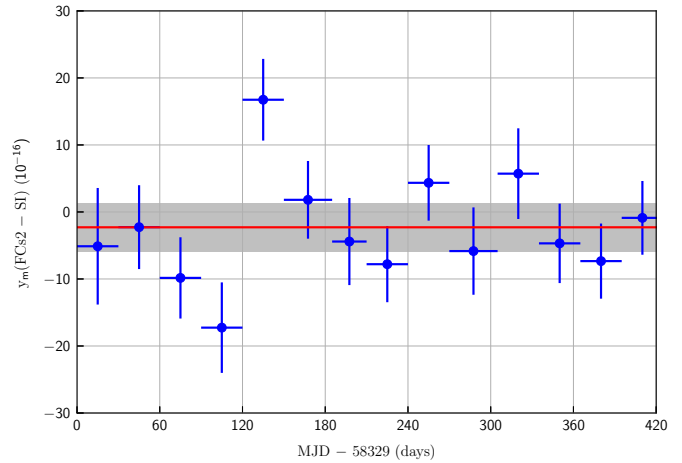


**Figure 15.** Frequency difference between the NRC-FCs2 and the SI second. The vertical error bars are the uncertainty for each frequency comparison period. The red line denotes the overall weighted mean ($-2.4(3.7)\times 10^{-16}$) with the grey area indicating the combined systematic and statistical uncertainty. The horizontal error bars indicate the frequency comparison periods.

[50]. The frequency difference between the full measurement period and the fountain up-time was calculated for each data set. The standard deviation of the frequency differences was used as the dead time uncertainty.

The frequency transfer from VM1 to TAI through the GPS link was evaluated using the UTC−UTC(NRC) data from the Circular T for a period of 530 days, beginning April 2018 [51]. The phase data at each part of the link from VM1 to TAI (VM1→UTC(NRC)→TAI) on the TAI 5-day time grid was used to calculate the fractional frequency difference, y(VM1-TAI), and the average frequency difference at the midpoint of each data group, $y_m$(VM1-TAI). We found that VM1 experiences a settling in its frequency drift rate and y(VM1-TAI) could be fitted accurately using a third-order polynomial function. The link uncertainties from VM1 to TAI, $u_{l/TAI}$, were found from the Allan deviation of the phase difference with the maser drift removed, giving a value of $3.1 \times 10^{-16}$ for the typical 30-day duration. This uncertainty was expanded to $u_{l/\text{TAI}} = 4.1 \times 10^{-16}$ to account for discrepancies between measured frequencies from different GPS receivers.

The average frequency difference between NRC-FCs2 and TAI for each data group was calculated as $y_m$(FCs2-TAI) = $y_m$(FCs2-VM1) + $y_m$(VM1-TAI). To compare to the SI second, TAI was corrected using the scale interval *d*, which is estimated from the reported primary and secondary frequency standards for any given Circular T period. Figure 15 shows the monthly frequency difference between NRC-FCs2 and the SI second, $y_m$(FCs2-SI) = $y_m$(FCs2-TAI) - *d*, from August 2018 to September 2019. The uncertainty of *d* includes systematic and statistical uncertainties, as well as the frequency transfer uncertainties stated in the Circular T publication. The weighted average $y_m^{\text{avg}}$(FCs2-SI) = ($-2.4 \pm 3.4$ (syst.) $\pm$ 1.4 (stat.)) $\times 10^{-16}$ is obtained for the frequency comparison period of fourteen months with a reduced chi-square of $\chi^2 = 1.7$. The systematic uncertainty, which we assume does

not average down over time, is a combination of the overall systematic uncertainty of NRC-FCs2 and that of $d$ over the 14-month measurement ($1.0 \times 10^{-16}$) [52]. The data taken in November and December 2018 (MJD 58419-58479) show significant deviations from the average. However, during this period a number of changes were made to the frequency synthesis chain. Since that period, NRC-FCs2 has shown reliable performance with $\chi^2 = 0.9$ for our frequency comparisons with the SI second. It should also be noted that the physics package tilt angle was optimized using various methods during the measurement. However, the angle was always within 1 mrad of our optimal angle, and consequently, any change in the DCP frequency bias due to changes in tilt angle will be well below the stated uncertainty for NRC-FCs2.

## 5. Conclusions

We report the first accuracy evaluation of NRC-FCs2, a primary frequency standard developed at the National Research Council Canada. NRC-FCs2 has been operating since August, 2018. During this time it has run in a number of configurations to characterize the systematic shifts. It now runs increasingly in standard operating mode with long measurement times ((10–20) days) and minimal unscheduled downtime. The overall type B uncertainty is $2.3 \times 10^{-16}$ and the type A uncertainty is $\sim 1.7 \times 10^{-13}$ after one second of averaging. NRC-FCs2 agrees with other fountains worldwide through GPS comparisons, with a measured difference of $-2.4(3.7) \times 10^{-16}$. NRC-FCs2 will serve as a primary frequency standard for Canada and contribute to the steering of TAI.

## Acknowledgments

## ORCID iDs

Scott Beattie https://orcid.org/0000-0003-2056-2871
Bin Jian https://orcid.org/0000-0002-4588-3957
Marina Gertsvolf https://orcid.org/0000-0002-1188-2104
Rich Hendricks https://orcid.org/0000-0002-5518-3719
Krzysztof Szymaniec https://orcid.org/0000-0002-3523-278X
Kurt Gibble https://orcid.org/0000-0003-3652-9638

## References

[1] Clairon A, Laurent P, Santarelli G, Ghezali S, Lea S N and Bahoura M 1995 *IEEE Trans. Instrum. Meas.* **44** 128–31
[2] Wynands R and Weyers S 2005 *Metrologia* **42** S64
[3] Gerginov V, Nemitz N, Weyers S, Schröder R, Griebsch D and Wynands R 2010 *Metrologia* **47** 65–79
[4] Szymaniec K, Park S E, Marra G and Chalupczak W 2010 *Metrologia* **47** 363–76
[5] Li R, Gibble K and Szymaniec K 2011 *Metrologia* **48** 283–9
[6] Guéna J *et al* 2012 *IEEE Trans. Ultrason. Ferroelectr. Freq. Control* **59** 391–410
[7] Domnin Y S, Baryshev V N, Boyko A I, Elkin G A, Novoselov A V, Kopylov L N and Kupalov D S 2013 *Meas. Tech.* **55** 1155–62
[8] Levi F, Calonico D, Calosso C E, Godone A, Micalizio S and Costanzo G A 2014 *Metrologia* **51** 270–84
[9] Weyers S, Gerginov V, Kazda M, Rahn J, Lipphardt B, Dobrev G and Gibble K 2018 *Metrologia* **55** 789–805
[10] Heavner T P, Donley E A, Levi F, Costanzo G, Parker T E, Shirley J H, Ashby N, Barlow S and Jefferts S R 2014 *Metrologia* **51** 174–82
[11] Beattie S, Alcock J, Jian B, Gertsvolf M and Bernard J 2016 *J. Phys.: Conf. Ser.* **723** 012008
[12] Dubé P, Madej A A, Zhou Z and Bernard J E 2013 *Phys. Rev. A* **87** 023806
[13] Dubé P, Bernard J E and Gertsvolf M 2017 *Metrologia* **54** 290
[14] Szymaniec K, Lea S N, Gibble K, Liu K and Glowacki P 2016 *J. Phys.: Conf. Ser.* 012003
[15] Hendricks R, Ozimek F, Szymaniec K, Nagorny B, Dunst P, Nawrocki J, Beattie S, Jian B and Gibble K 2018 *IEEE Trans. Ultrason. Ferroelectr. Freq. Control* **66** 624–31
[16] Li R and Gibble K 2010 *Metrologia* **47** 534–51
[17] Gibble K, Lea S N and Szymaniec K 2012 *Conf. on Precision Electromagnetic Measurements* pp 700–1
[18] Snyder J J, Raj R K, Bloch D and Ducloy M 1980 *Opt. Lett.* **5** 163–5
[19] Breit G and Rabi I I 1931 *Phys. Rev.* **38** 2082–3
[20] Vanier J and Audoin C 1989 *The Quantum Physics of Atomic Frequency Standards* vol 2 (Bristol: Institute of Physics Publishing)
[21] Itano W, Lewis L L and Wineland D J 1982 *Phys. Rev.* A **25** 1233–5
[22] Beloy K, Safronova U I and Derevianko A 2006 *Phys. Rev. Lett.* **97** 040801
[23] Angstmann E J, Dzuba V A and Flambaum V V 2006 *Physical Review A* **74** 023405
[24] Kokkelmans S J J M F, Verhaar B J, Gibble K and Heinzen D J 1997 *Phys. Rev.* A **56** R4389–R4392
[25] Fertig C and Gibble K 2000 *Phys. Rev. Lett.* **85** 1622
[26] Sortais Y, Bize S, Nicolas C, Clairon A, Salomon C and Williams C 2000 *Phys. Rev. Lett.* **85** 3117
[27] Fang F *et al* 2015 *Metrologia* **52** 454–68
[28] Kumagai M, Ito H, Kido K, Shiga N, Kajita M, Hartnett J G and Hanado Y 2016 *2016th Conf. on Precision Electromagnetic Measurements (CPEM 2016)* pp 1–2
[29] Szymaniec K, Chalupczak W, Tiesinga E, Williams C J, Weyers S and Wynands R 2007 *Phys. Rev. Lett.* **98** 153002
[30] Szymaniec K and Park S E 2011 *IEEE Trans. Instrum. Meas.* **60** 2475–81
[31] Gibble K 2013 *Phys. Rev. Lett.* **110** 180802
[32] Li R and Gibble K 2004 *Metrologia* **41** 376–86
[33] Guéna J, Li R, Gibble K, Bize S and Clairon A 2011 *Phys. Rev. Lett.* **106** 130801
[34] Gibble K 2006 *Phys. Rev. Lett.* **97** 073002
[35] Fang F, Liu K, Chen W L, Nian-Feng L, Suo R and Li T C 2014 *Chin. Phys. Lett.* **31** 100601
[36] Weyers S, Schröder R and Wynands R 2006 *Proc. of the 20th European Frequency and Time Forum* pp 173–80
[37] Shirley J H, Levi F, Heavner T P, Calonico D, Yu D H and Jefferts S R 2006 *IEEE Trans. Ultrason. Ferroelectr. Freq. Control* **53** 2376–85
[38] Audoin C, Jardino M, Cutler L S and Lacey R F 1978 *IEEE Trans. Instrum. Meas.* **27** 325–9

[39] Levi F, Shirley J H, Heavner T P, Yu D H and Jefferts S R 2006 *IEEE Trans. Ultrason. Ferroelectr. Freq. Control* **53** 1584–9

[40] Cutler L S, Flory C A, Giffard R P and De Marchi A 1991 *J. Appl. Phys.* **69** 2780–92

[41] Wynands R, Schroder R and Weyers S 2007 *IEEE Trans. Instrum. Meas.* **56** 660–3

[42] Santarelli G *et al* 2009 *IEEE Trans. Ultrason. Ferroelectr. Freq. Control* **56** 1319–26

[43] Silliker J and Belzile A 2011 Height difference for the strontium ion optical frequency standard at the National Research Council of Canada Tech. rep. Natural Resources Canada

[44] https://www.bipm.org/en/bipm-services/timescales/time-ftp/Circular-T.html

[45] Yu D H, Weiss M and Parker T E 2007 *Metrologia* **44** 91

[46] Hachisu H and Ido T 2015 *Japan. J. Appl. Phys.* **54** 112401

[47] Leute J *et al* 2016 *IEEE Trans. Ultrason. Ferroelectr. Freq. Control* **63** 981–5

[48] Baynham C F *et al* 2018 *J. Mod. Opt.* **65** 585–91

[49] Grebing C *et al* 2016 *Optica* **3** 563–9

[50] https://ieee-uffc.org/frequency-control/frequency-control-software/stable32/

[51] Petit G and Panfilo G 2018 *Proc. 2018 European Frequency and Time Forum (EFTF)* 185–7

[52] McGrew W F *et al* 2019 *Optica* **6** 448–54